POLITECNICO DI TORINO
Repository ISTITUZIONALE

Contactless Air–Filled Substrate Integrated Waveguide on Low–Cost PCB for D–Band Applications

Original
Contactless Air–Filled Substrate Integrated Waveguide on Low–Cost PCB for D–Band Applications / Aktas, K., Petek, M., Tolin, E., Bruni, S., Vasquez, J.A.T., Vipiana, F.. - In: IEEE TRANSACTIONS ON COMPONENTS, PACKAGING AND MANUFACTURING TECHNOLOGY. PART C. MANUFACTURING. - ISSN 1083-4400. - 16:10(2026), pp. 2347-2359. [10.1109/tcpmt.2026.3717541]

Availability:
This version is available at: 11583/3015293 since: 2026-09-08T14:21:21Z

Publisher:
IEEE

Published
DOI:10.1109/tcpmt.2026.3717541

Terms of use:

This article is made available under terms and conditions as specified in the corresponding bibliographic description in the repository

Publisher copyright

(Article begins on next page)

20 November 2026

Contactless Air-Filled Substrate Integrated Waveguide on Low-Cost PCB for D-Band Applications

Kaan Aktaş, *Graduate Student Member, IEEE*, Martin Petek, *Member, IEEE*, Enrico Tolin, Simona Bruni, *Member, IEEE*, Jorge Alberto Tobón Vásquez, and Francesca Vipiana, *Senior Member, IEEE*

***Abstract*—D-band radar systems offer significant advantages for automotive applications, including large bandwidth for high-precision object detection in crowded environments and compact solutions. However, their widespread adoption is hindered by significant transmission losses and high manufacturing costs in conventional transmission line technologies. This article addresses these challenges by introducing a novel, cost-effective contactless air-filled substrate integrated waveguide (CLAFSIW) design for the 134–148.5-GHz frequency range. It features an E-bend vertical transition allowing for compact integration with next-generation monolithic microwave integrated circuit radars. Fabricated using a standard FR4 printed circuit board (PCB), the design is suitable for mass production. The prototype board demonstrates excellent performance close to simulation predictions despite manufacturing discrepancies. Measurements confirm an average insertion loss of 0.037 dB/mm with a back-to-back transition matching below −10 dB across the desired band. The design also exhibits high isolation, with crosstalk between adjacent CLAFSIW lines remaining below −26 dB.**

***Index Terms*—Automotive applications, D-band, electromagnetic band gap, gap waveguide, microwave bends, microwave integrated circuits, millimeter wave radar, periodic structures, transmission lines.**

I. Introduction

WIDEBAND compact radar systems are becoming critical for emerging advanced driver assistance systems (ADASs), offering two key benefits: resilience to environmental conditions (temperature, air currents, darkness, etc.) [1], and high-resolution object detection with richer data for enhanced artificial intelligence shape recognition [2], [3]. Within the latter scope, the 76–81-GHz band has been introduced in Europe and the United States to replace the traditional 24-GHz ultra-wideband [4]. However, due to the increasing number of radar implementations in newer vehicles, it is expected that this new band will soon be congested, hence increasing the interference from other radar systems operating in the same frequency range [5]. Consequently, the D-band is being actively investigated in Europe, with potential frequency allocations spanning 122.25–130 GHz, 134–141 GHz, and 141–148.5 GHz [6].

Operating at D-band offers more compact and larger bandwidth antenna designs, leading to higher precision in distinguishing targets in crowded environments [3], [7]. Although D-band offers significant advantages, traditional transmission line technologies encounter substantial performance limitations at these frequencies. The demand for cost-effective solutions in the automotive industry also presents a key challenge. Waveguides, despite their low-loss characteristics [8], suffer from costly production due to their small size and the need for diffusion bonding to prevent signal leakage from gaps [9], [10]. Additive manufacturing provides a cost-effective alternative [11], [12]; nevertheless, achieving industrial-scale mass production remains a challenge. Microstrip lines, while offering a cheaper solution using printed circuit board (PCB) fabrication, introduce additional loss due to the dielectric itself. Furthermore, at higher frequencies, they incur radiation loss caused by fringing fields and surface currents. This not only degrades efficiency but also exacerbates crosstalk [10], [13], [14]. Among other PCB technologies, substrate integrated waveguides (SIWs), utilizing closely spaced vias to emulate metallic walls, offer a lower radiation loss. Although well-established in D-band applications [15], [16], [17], [18], [19], achieving higher transmission requires costly low-loss dielectric materials for the substrate [20]. These dielectric losses may be mitigated by using an air-filled SIW (AFSIW). However, ensuring perfect contact between the metallic plates and the substrate requires complex methods using laser cutting or soldering [21], [22].

A promising alternative is gap waveguide technology [9], as it offers the advantage of diminished radiation and dielectric loss, even with nonuniform gap formation within its structure. Metallic gap waveguides in D-band applications are most commonly based on either pin [23], [24], [25], [26], [27], [28] or holey electromagnetic bandgap (EBG) structures [29].

Received 18 May 2026; accepted 20 July 2026. Date of publication 30 July 2026; date of current version 21 October 2026. This work was supported in part by the Horizon Europe Research and Innovation Program under the GENIUS Project under Grant GA101072560 and in part by the Project MedWaveImage funded by Interreg Central Europe under Grant CE0200670. Recommended for publication by Associate Editor F. Wei upon evaluation of reviewers' comments. *(Corresponding author: Francesca Vipiana.)*

Kaan Aktaş is with the Department of Electronics and Telecommunications, Politecnico di Torino, 10129 Turin, Italy, and also with IMST GmbH, 47475 Kamp-Lintfort, Germany (e-mail: kaan.aktas@polito.it).

Martin Petek, Jorge Alberto Tobón Vásquez, and Francesca Vipiana are with the Department of Electronics and Telecommunications, Politecnico di Torino, 10129 Turin, Italy (e-mail: martin.petek@polito.it; jorge.tobon@polito.it; francesca.vipiana@polito.it).

Enrico Tolin and Simona Bruni are with IMST GmbH, 47475 Kamp-Lintfort, Germany (e-mail: enrico.tolin@imst.de; simona.bruni@imst.de).

Digital Object Identifier 10.1109/TCPMT.2026.3717541

© 2026 The Authors. This work is licensed under a Creative Commons Attribution 4.0 License.
For more information, see https://creativecommons.org/licenses/by/4.0/

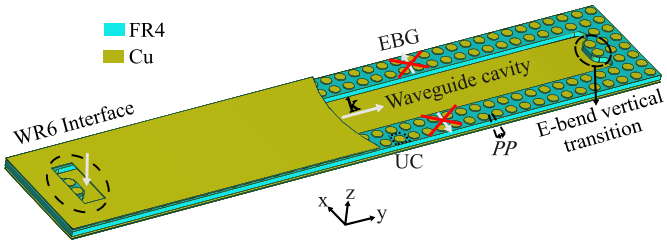


Fig. 1. Conceptual illustration of the proposed D-band CLAFSIW design. Dashed black line: WR6 aperture and E-bend vertical transition. Silver arrow: direction of the wave vector **k**. Red cross: propagation cancellation in any direction. Yellow: copper (Cu). Blue: FR4 substrate. Pad-to-pad distance (*PP*). Dotted square: UC.

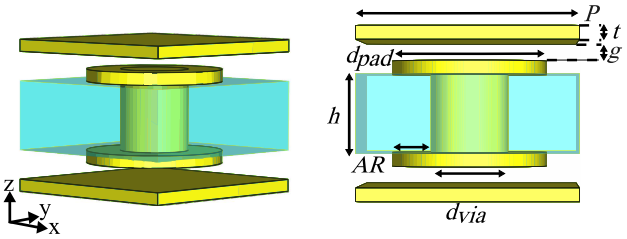


Fig. 2. (a) and (b) represent 3D and side view of UC design respectively. UC parameters: periodicity (*P*), annular ring width (*AR*), pad diameter (d_{pad}), via diameter (d_{via}), substrate height (*h*), gap size (*g*), and copper thickness (*t*).

While metallized plastic injection molding is an existing low-cost industrial option [30], PCB-based implementations offer direct integration with circuit components. Within PCB-based gap waveguide designs, substrate integrated hole (SIH) unit cells (UCs) [31], [32], [33] and mushroom-type UCs can be used as EBG structures [34], [35], [36], [37], [38], [39], [40]. Existing gap waveguide designs of both types generally operate at lower frequencies, with very limited literature available in the D-band range. To the best of the authors' knowledge, there is no practical implementation of a PCB-based gap waveguide functioning at D-band. Only in [41] is a D-band UC proposed for flange leakage suppression. However, this UC is constructed on a three-layer PCB. This conflicts with our objective of avoiding multilayer solutions, as it significantly increases fabrication complexity compared to a double-layer PCB design with a single laminate.

The key novelty of this article is the introduction of the first D-band gap waveguide based on standard PCB manufacturing. The proposed design in Fig. 1 demonstrates, to the best of the authors' knowledge, for the first time a solution using FR4 material to bridge the gap between stringent D-band performance requirements and low-cost, mass-production scalability [1] within the existing PCB standards of the automotive industry. As automotive radars transition toward sub-THz frequencies, maintaining compatibility with conventional PCB processes is critical for commercial viability. This industrial requirement drives the selection of FR4 substrate over costly, specialized microwave substrates [42], [43], [44]. Despite the challenges of its high dielectric loss, frequency-dependent material properties, and PCB fabrication tolerances at D-band, our design manages these limitations and provides a wideband transmission line specifically targeting the 134–148.5-GHz frequency range. It presents a suitable solution for interconnects and feed networks of radar front-ends established in EBG [23], [24], [25], [26], [45], and SIW structures [15], [16], [17], [18].

Unlike SIH UCs, which require a high number of vias to define a hole perimeter (potentially complicating design and manufacturing), the proposed EBG design adapts the mushroom-type UC of the contactless, air-filled SIW (CLAFSIW). This type of UC offers a significant advantage for achieving higher frequency operation due to its minimal periodicity, realized by a central via surrounded by a dielectric. While previously demonstrated at lower frequencies [35], [36], [37], [38], this work presents the first successful implementation of contactless air-filled SIW (CLAFSIW) to the D-band, within the constraints of conventional manufacturing and high dielectric losses. In addition, its stopband has been characterized through the application of the multimodal transfer matrix method (MMTMM). This method allows for evaluating the stopband attenuation, which is not currently available in commercial eigenmode solvers (ESs) [46], [47], [48], [49].

Furthermore, we incorporate an E-bend vertical transition into our CLAFSIW design for its compatibility with the waveguide launchers used in current automotive radar microchips [44], [45], [50]. Our via-based solution allows for a design on a single laminate, providing better adaptability for mass production compared to multilayer solutions [15], [16], [17]. In the context of this study, however, this transition serves only as a characterization interface for measurements, specifically designed to provide a stable and repeatable connection between the CLAFSIW and the measurement equipment.

This article is organized as follows. Section II introduces the proposed UC, including its dispersion diagram and MMTMM analysis. It then details the vertical transition-integrated straight CLAFSIW line and its performance, specifically targeting the 134–148.5-GHz band for radar microchip applications. Section III describes the prototype realization and the thru-reflect-line (TRL) calibration measurements and coupling characteristics. Finally, Section IV concludes this article and outlines future perspectives.

II. CLAFSIW Design and Analysis

A. UC Design and Parametric Study

In this section, we analyze the stopband sensitivity of a double-sided mushroom-type UC, shown in Fig. 2, considering fabrication tolerances in the 134–148.5-GHz range. The design is implemented with a 200-μm thick Panasonic FR4 substrate (ϵ_r = 4.7 and tanδ = 0.01) [51] using standard 35-μm copper cladding. A 50-μm air gap is considered to account for maximum anticipated assembly tolerance between the pads and parallel plates [38]. Unlike square pads [35], circular shapes are used to minimize the capacitance effect, hence reaching higher frequencies.

The UC is arranged in a square lattice with a subwavelength periodicity to achieve a compact design. To balance compactness with the PCB manufacturing limitations

TABLE I
UC DESIGN PARAMETERS AND DIMENSIONS WITHIN FABRICATION CONSTRAINTS

Parameters (μm)	Min	Max	Final
P	500	673	560
PP	100	273	160
AR	100	186.5	100
d_{pad}	400	573	400
d_{via}	200	373	200
g	0	50	50

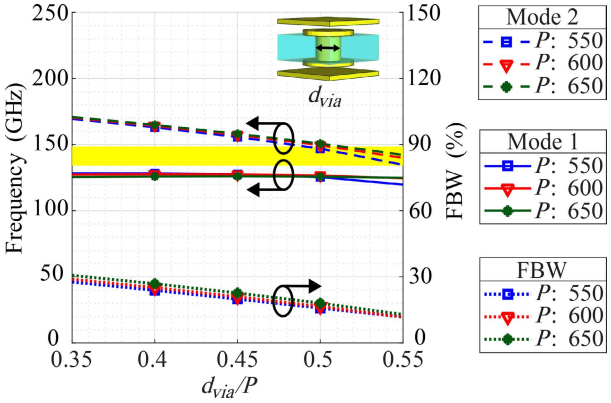


Fig. 3. UC dispersion diagram and FBW of the stopband regarding varying via diameter/period ratios for a range of periods. The yellow rectangle highlights the 134–148.5-GHz range. h: 200 μm, g: 50 μm, and AR: 100 μm. Inset: UC.

(e.g., pad spacing and dimensions), the periodicity is determined by $\lambda_g/4 < P < \lambda_g/3$ at 148.5 GHz. With UC dimensions in Table I, we now investigate the impact of key parameters on the UC's performance for various periods. For each case, we use an ES to determine the boundary modes of the stopband (modes 1 and 2), and calculate the fractional bandwidth (FBW).

For minimal radiation loss in CLAFSIW technology, an approximate 50% via diameter to period ratio is suggested in [35]. However, this requirement leads to a barely sufficient stopband for the desired band as shown in Fig. 3, resulting in greater sensitivity to manufacturing variations. Consequently, the smallest achievable via diameter (200 μm) is selected to maximize the stopband and enhance tolerance to variations in gaps and pad sizes.

As shown in Fig. 4, the stopband center frequency (f_c) is inversely proportional to pad size, explained with the LC resonance model in [34]. The target stopband is maintained for pad diameters between 380 and 440 μm ($1.9 < d_{pad}/d_{via} < 2.2$), highlighting high sensitivity to PCB manufacturing tolerances. For a smaller periodicity, the bandwidth changes at a higher rate within this range. To illustrate these trends, Fig. 4 includes parameter values exceeding Table I constraints.

Fig. 5 demonstrates that the substrate height, h, can be used as a tuning parameter to shift the stopband central frequency without significantly degrading the bandwidth like other parameters. For this design, h is fixed at a standard 200 μm, though sensitivity analysis confirms the stopband

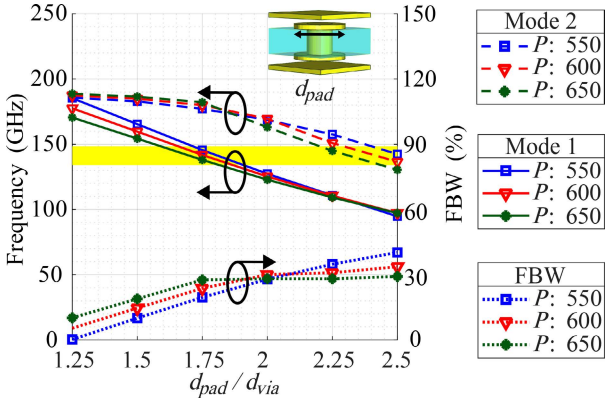


Fig. 4. Dispersion diagrams at d_{via}: 200 μm, h: 200 μm, and g: 50 μm. Varying circular pad/via diameter ratios at different periods, including FBW. The yellow rectangle depicts the 134–148.5-GHz range. Inset: UC.

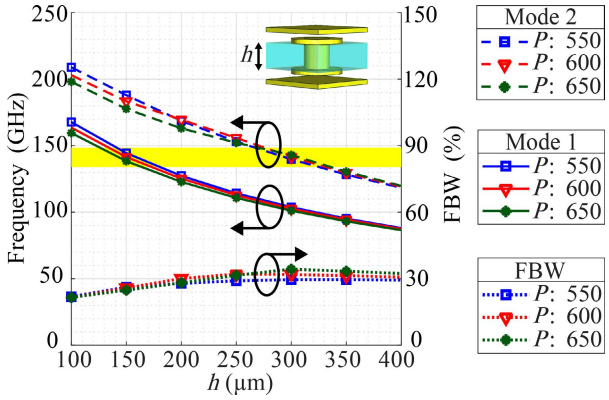


Fig. 5. Dispersion diagram for various substrate heights at different periods including FBW. The yellow rectangle indicates the 134–148.5-GHz band. Inset: UC. d_{via}: 200 μm, d_{pad}: 400 μm, and g: 50 μm.

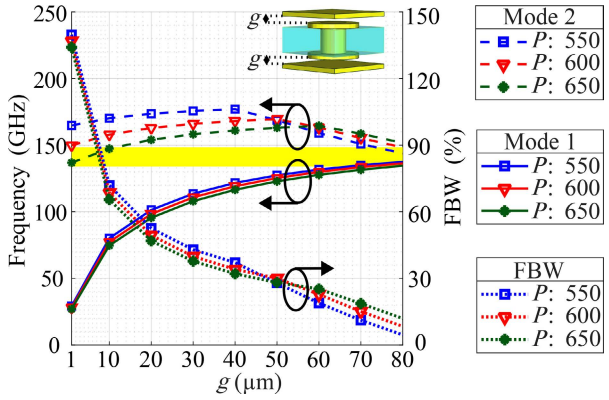


Fig. 6. Dispersion diagram for various gap sizes across a range of periods including FBW. The yellow rectangle shows the 134–148.5-GHz range. Inset: UC. h: 200 μm, d_{via}: 200 μm, and d_{pad}: 400 μm.

remains compliant even with $\pm 10\%$ height variations. While this thickness is at the lower end of conventional FR4 laminate profiles, it is essential to operate in the D-band range and still provides a cheaper solution than using specialized RF materials [45].

As shown in Fig. 6, the stopband bandwidth decreases with increasing gap size (g). Since the gap size is expected to be

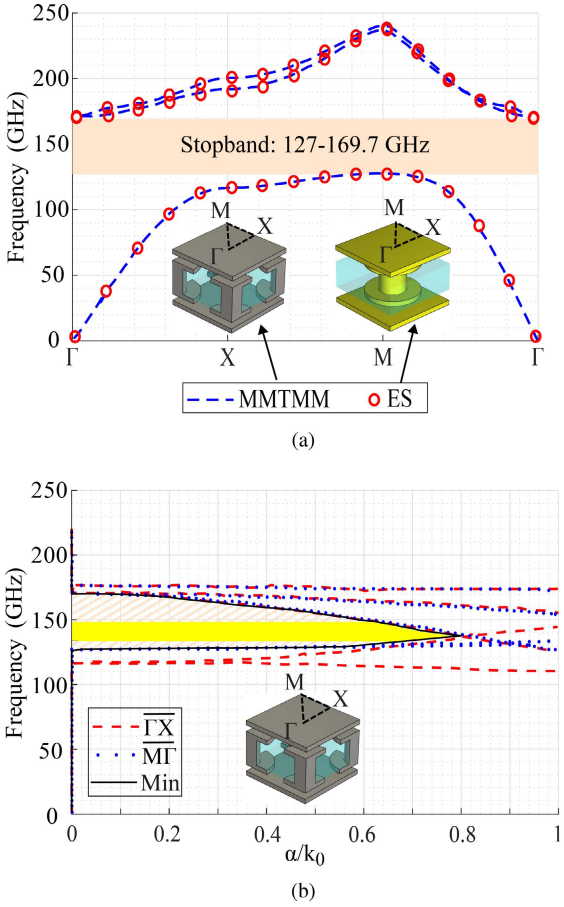


Fig. 7. Analysis of the proposed UC from different Brillouin zone perspectives, used for ES and MMTMM calculations within the same lattice. (a) Full dispersion diagram for the first three modes with stopband highlighted between modes 1 and 2 with an orange rectangle. (b) Normalized attenuation constant achieved with MMTMM for the $\overline{\Gamma X}$ and $\overline{M\Gamma}$ regions. Black outline and orange diagonal lines highlight the minimum attenuation region in any direction. The yellow region denotes the 134–148.5-GHz frequency range.

nonuniform across the assembled structure, the 550-μm period is advantageous to ensure the largest FBW and also a compact design.

The finalized UC dimensions (see Table I) are adapted for integration of the subsequent vertical transitions and matching performance by adjusting the period and the pad diameter to 560 and 400 μm, respectively (see Section II-B). To gain a complete understanding of the UC stopband properties, we use the MMTMM [49] with the first nine modes per port. Following the recommendations in [49], we define the computational domain used with the MMTMM as in the inset of Fig. 7.

Real-valued solutions show excellent agreement between the ES and the MMTMM in Fig. 7(a), confirming a stopband from 127 to 169.7 GHz with 28.8% FBW. Stopband attenuation analysis in Fig. 7(b) reveals a sharp increase above 127 GHz, with normalized attenuation values reaching 0.63–0.8 across all propagation directions within the operational band. Therefore, we expect the EBG structure to effectively suppress leakage within two and three rows as demonstrated in a previous work [47].

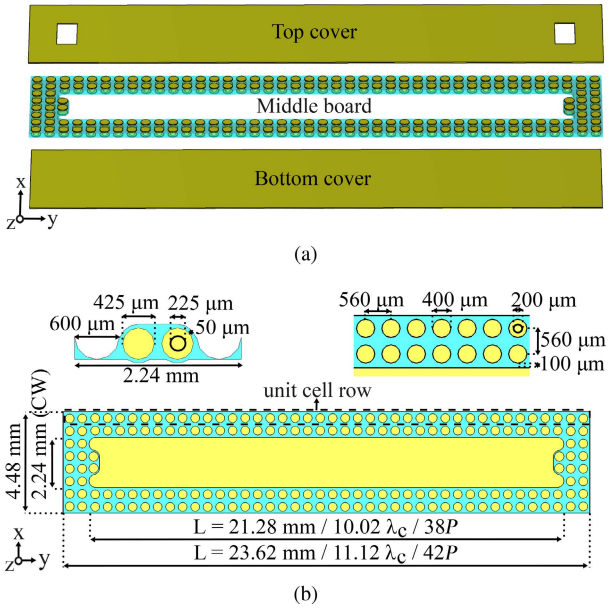


Fig. 8. Detailed CLAFSIW structure. (a) Layer-by-layer decomposition. (b) Top view of the middle layer showing waveguide channel, matching structure (top-left), and EBG segment (top-right) with detailed dimensions. CW: channel width.

B. Straight CLAFSIW Design With E-Bend Vertical Transition

The proposed CLAFSIW concept is illustrated in Fig. 1. Simulations are performed using the FDTD solver of the EMPIRE software [52] by considering a uniform gap size throughout the entire structure. As detailed in Fig. 8(a), the structure features three segments: metallic top and bottom covers and a middle FR4 layer. The top cover incorporates two WR6 waveguide apertures, while the middle layer features a two-row UC frame placed around the waveguide cavity and a vertical transition placed beneath the apertures. A 100-μm edge clearance is maintained between the pads and the waveguide cavity [Fig. 8(b)]. This minimum spacing ensures compliance with manufacturing constraints and minimizes the interaction of the wave with the lossy substrate.

To integrate the vertical transition while accommodating 600-μm drilling constraints and optimize CLAFSIW efficiency, the waveguide channel width (CW) is designed larger than standard WR6 dimensions. The simulation in Fig. 9 demonstrates that the configuration with four times the UC periodicity maintains the optimal transmission performance across gap sizes of 10–50 μm, with $|S_{21}| > -0.53$ dB over a $10\lambda_c$ segment. Here, λ_c is the wavelength at f_c (i.e., 141.25 GHz) of the target band. At a 50-μm gap, the design achieves an average transmission loss of 0.017 dB/mm calculated over this frequency range.

The vertical transition utilizes two vias [see top left of Fig. 8(b)] with a 50-μm clearance, the minimum limit for mechanical drilling. As shown in Fig. 10, this dual-via configuration provides optimal transmission across the 134–148.5-GHz band. Therefore, to satisfy CW requirements and drilling tolerances for the transition, the UC period is

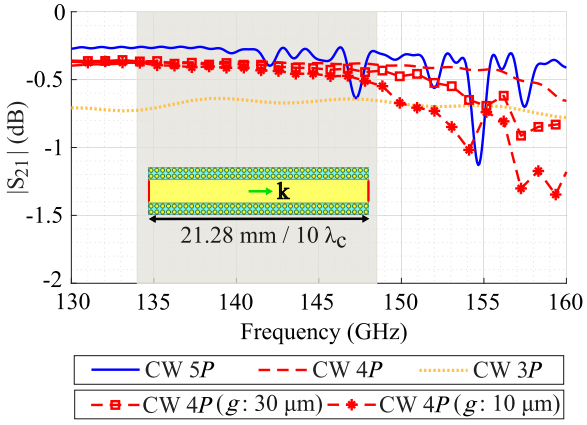


Fig. 9. S_{21} amplitude for varying CWs (multiples of UC periodicity P) at g: 50 μm, with additional gap sizes (10 and 30 μm) for the $4P$ width. The gray region indicates the operating band. Inset: $10\lambda_c$ CLAFSIW simulation model fed from the sides using final UC dimensions in Table I. Port placements in red rectangles. **k**: wave vector. For all configurations, $|S_{11}| < -19$ dB across 130–160 GHz.

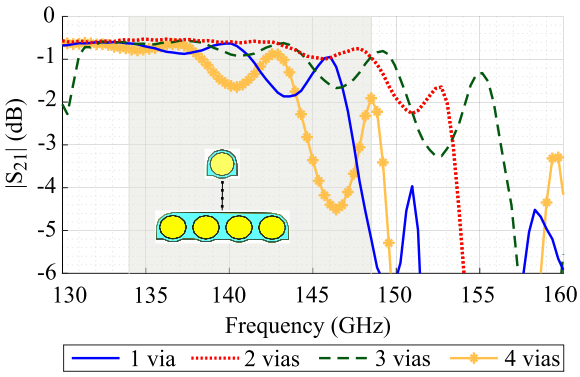


Fig. 10. Comparative analysis of transmission performance for various via quantities in the vertical transition of the CLAFSIW design in Fig. 8. Inset depicts vertical transitions with 1 via and 4 vias. g: 50 μm.

increased from 550 to 560 μm (see Table I), thereby widening the waveguide channel.

Since via dimensions and spacing of the transition are nearly at the minimum of manufacturing limits (see Table I), impedance matching is improved by also tuning the UC pad size. Fig. 11 compares two CLAFSIW designs using UCs UC_1 and UC_2 (pad sizes: 425 and 400 μm) while the vertical transition is fixed at a pad size of 425 μm. UC_2 provides superior matching with $|S_{11}| < -10$ dB and $|S_{21}| > -1$ dB while retaining the full stopband coverage over the entire band of interest.

All of these adjustments led to the final CLAFSIW design shown in Fig. 8 with performance indicated in Fig. 11 at a 50 μm gap for a $10\lambda_c$ length. The electric field distributions are presented in Fig. 12, demonstrating the structure's effectiveness in performing the vertical transition and mitigating leakage from the gaps, hence effectively confining waves within the waveguide channel with two rows of UCs only.

III. Prototype Measurements and Discussion

In this section, we experimentally validate and characterize the proposed CLAFSIW design by analyzing its performance

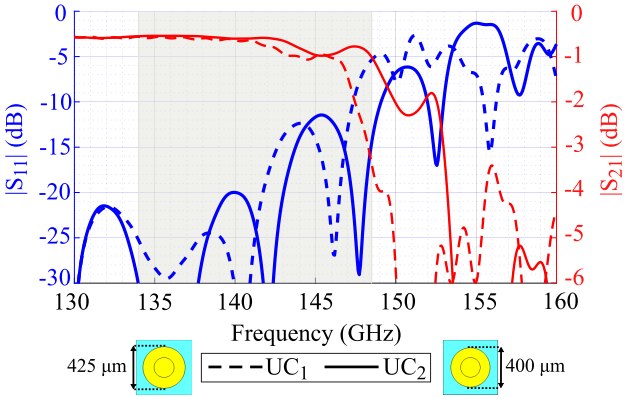


Fig. 11. Matching comparison between mid-band (UC_1) and implemented (UC_2) UCs having 425- and 400-μm pad diameters, respectively. Inset depicts UC pad size. g: 50 μm.

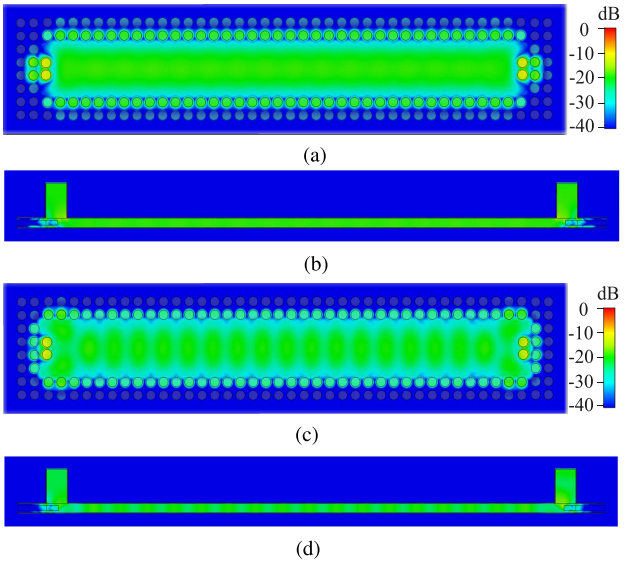


Fig. 12. Electric field distributions at maximum amplitude with a normalized dB scale shown from top (XY) and side (YZ) plane views. (a) XY plane view at 134 GHz. (b) YZ plane view at 134 GHz. (c) XY plane view at 148.5 GHz. (d) YZ plane view at 148.5 GHz.

across different lengths and applying TRL de-embedding to understand the associated losses. Note that, in the simulations, we consider a uniform gap size across the entire model. In addition, we examine the suppression of coupling between two adjacent waveguides in relation to the number of UCs at the intersection. The latter analysis becomes important when multiple CLAFSIWs carrying different signals are fabricated on the same substrate and placed in close proximity.

A. Prototype Board Organization

We first begin by explaining in detail the organization of the prototype board. It is composed of a stacked configuration of three independent boards: top, middle, and bottom. The top and bottom boards are the PCB realization of the top and bottom copper covers in Fig. 8(a). The assembled configuration is shown in Fig. 13, detailing how the components are integrated. Each individual board is a double-sided PCB with bare copper separated by a coating material that maintains a gap. Note

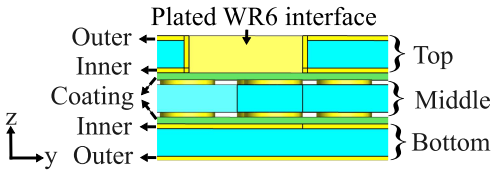


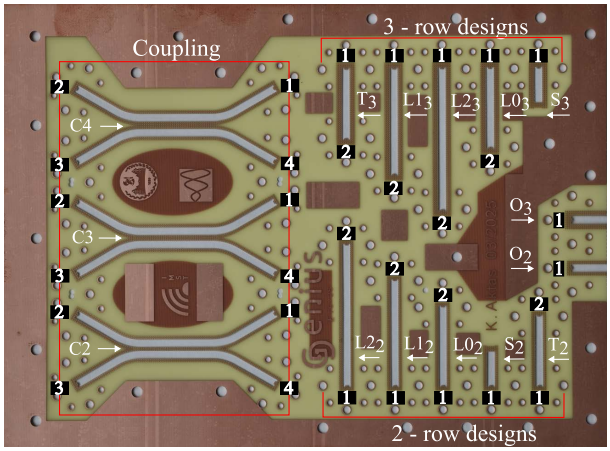
Fig. 13. Side view of the prototype board showing its decomposition.

TABLE II
WAVEGUIDE CHANNEL LENGTHS OF MANUFACTURED DESIGNS

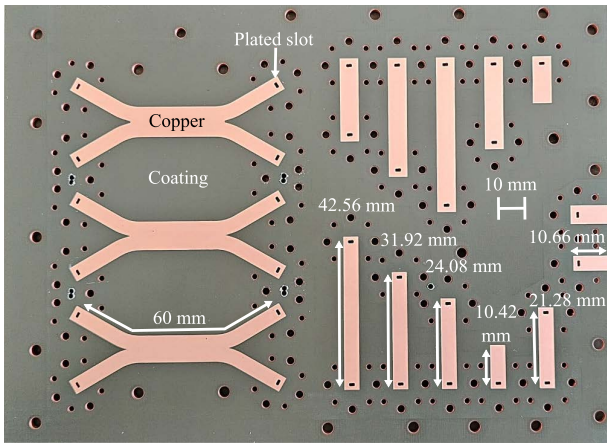
Designs	Length (mm)	Length (λ_c)
T	21.28	10
S	10.42	4.9
L0	24.08	11.3
L1	31.92	15
L2	42.56	20
C	60	28.2
O	10.66	5.02

that the material does not cover the pads and the waves are significantly attenuated before reaching the coating interface, yielding a negligible impact on CLAFSIW performance. The rectangular copper-plated slot is designed to accommodate the WR6 flange. The three boards are screwed together to constitute the final prototype board. Since the CLAFSIW design is fully enclosed, no additional surface finishing is applied for oxidation.

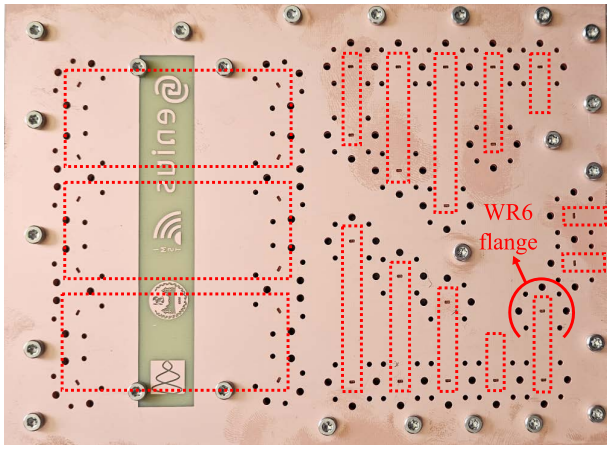
Each board is divided into three sections as depicted in Fig. 14(a): coupling, two-row, and three-row designs. The *N*-row sections contain designs where the waveguide cavity is surrounded by *N* rows of UCs, as exemplified in Fig. 8(b) for a two-row design. The middle board is shown in Fig. 14(a). It includes the waveguide cavities that are formed with a 600-μm drilling tool and all the vias used in EBG structures and vertical transitions. Each design is indicated with an arrow. The T CLAFSIW line, which stands for "thru," is the one explained in Section II-B. The L0, L1, and L2 lines are straight CLAFSIW designs as T with various lengths. "L" stands for "line" and the numbering is just to indicate the shortest to the longest length. The design S (for short) is intended to provide wave reflection with a load composed of EBG UCs placed at the end of the CLAFSIW. The open (O) design is intended for an open circuit; however, it is omitted from our analysis as the short design demonstrated superior reflection. The number at the subscript of each line is to represent how many UC rows are used (i.e., T_2 for two rows). Waveguide channel length of each design in terms of wavelength (λ_c) is listed in Table II. The three-row designs are structurally identical to two-row CLAFSIWs, but placed in different orders and use three UC rows to investigate whether an increase in rows influences the confinement of waves within the waveguide cavity. The numbering with white font and black background represents the excitation ports.



(a)



(b)



(c)

Fig. 14. Manufactured prototype boards, from middle-to-top board assembly order. (a) Middle board scheme with arrows indicating the designs. Thru (T), short (S), open (O), and lines (L) with a number indicating increasing length are shown. The subscript indicates the rows of UC (two or three). Port numbers are indicated with a white font on a black background. Coupling (C) with a number indicating the rows of UC at the intersection of two bent and mirrored CLAFSIW designs. (b) Top board inner surface and the waveguide cavity length of each design. (c) Top board outer surface where each design is highlighted with red dashed rectangles. Semicircle: WR6 flange mounting holes example.

On the left side of the board, coupling designs C2, C3, and C4 are placed. "C" stands for "coupling." Each incorporates a pair of intersecting mirrored CLAFSIW designs and allows

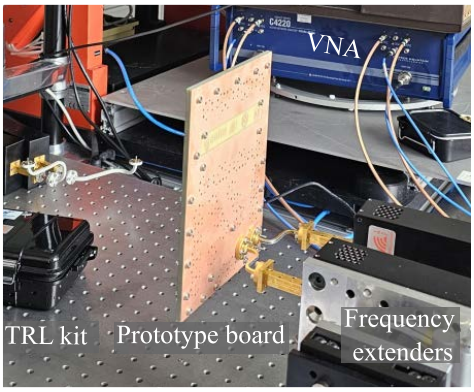


Fig. 15. Measurement setup showing the measurement of the straight CLAFSIW line T_2.

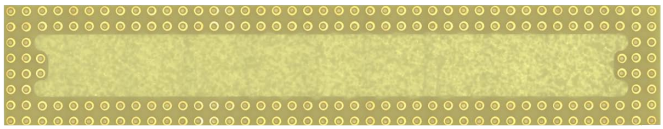


Fig. 16. Optical microscope view of T_2 straight CLAFSIW prototype on the middle board.

for investigating the ability of EBG structures to suppress the unwanted coupling. The numbering represents how many rows of UC are used at the intersection.

The inner surface of the top board is depicted in Fig. 14(b). The copper layer is co-plated with the outer surface and then covered with a PCB coating material. The remaining copper shapes function as the top and bottom covers for the vias and the cavities on the middle board. This creates the complete CLAFSIW structures, and their waveguide channel length is indicated by an arrow.

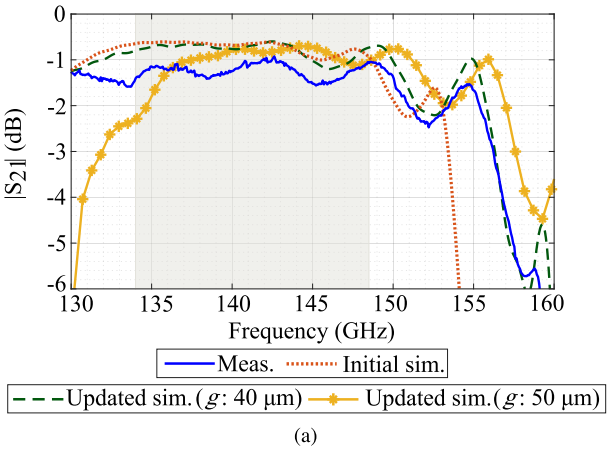
The outer surface of the top board is depicted in Fig. 14(c). The area where a WR6 flange is mounted is visible, with its corresponding holes marked by a red semicircle. Each individual design is demarcated by red dashed rectangles. Note that the bottom board has the same structure as the top board but is mirrored with respect to the z-axis and is without the slots.

Each CLAFSIW design on the prototype board is measured using a Vector Network Analyzer (VNA), as depicted in Fig. 15. The VNA ports are connected to frequency extenders to up-convert the signal to the D-band range. Both straight and S-bend waveguides are used to connect the extender ports to a CLAFSIW design. The VNA is calibrated with a standard TRL kit to remove the effects of the extenders and waveguides.

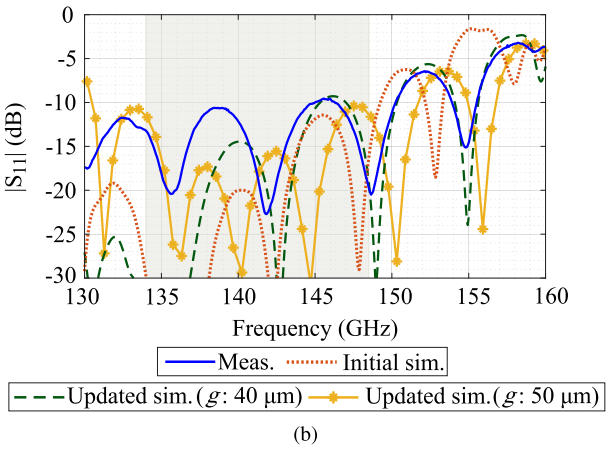
B. Straight CLAFSIW Prototype Analysis

In this section, we present an analysis of both the simulated and the measured performance of the straight CLAFSIW design T_2 shown in Fig. 16, following its detailed study in Section II.

As shown in Fig. 17, the measurements of the transmission and reflection parameters have a fair agreement with the initial simulation. However, the transmission parameter is shifted to higher frequencies by almost 2.5 GHz. These differences



(a)



(b)

Fig. 17. Comparison between measurements (meas.) and simulations (sim.) (a) transmission parameters and (b) reflection parameters. The "Initial sim." corresponds to the UC_2 results in Fig. 11. The "Updated sim." accounts for the updated design under prototype dimensions in Table III, assuming a uniform gap size of 40 and 50 μm across the structure.

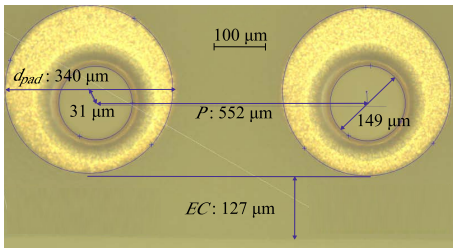


Fig. 18. Microscope image: dimensional measurement of the prototype.

indicate some manufacturing discrepancies, which we investigate with an optical microscope. A zoomed-in view of realized pads and vias is depicted in Fig. 18, with the dimensions clearly marked. The numerical ranges of dimensional errors are summarized in Table III. They affect the UC stopband and the matching of the vertical transition. Although they are in the acceptable range for standard PCB manufacturing, pad size is decreased by 15% from 400 to 340 μm. This smaller size reduces the capacitance and shifts the stopband of the UC and the matching to higher frequencies as predicted by the analysis in Fig. 11. However, this difference is balanced with an increased substrate height by 7.5% as shown in

TABLE III
DIMENSIONAL DISCREPANCIES BETWEEN DESIGN AND PROTOTYPE

Parameters (μm)	Initial sim.	Prototype	Updated sim.
P	560	550–555	555
d_{pad}	400	330–342	340
EC	100	100–140	140
h	200	215	215
t	35	39	39
g	50	-	40

Fig. 5. This explains the close relation between our initial simulation and measurements. Although the edge clearance varies by up to 40%, thereby increasing the dielectric content within the structure, this variation has a negligible impact on overall performance. This is primarily because the dielectric losses are significantly less dominant than ohmic losses in this design, a detailed breakdown of which is provided in the loss decomposition analysis in Section III-C.

Considering the results in Fig. 17, we note that the updated simulations assuming a 40-μm gap align the measurements closely. Due to the difficulties of measuring the exact gap size and its variance throughout the structure, we estimate with our simulations that its average value is in the range of 40–50 μm. Despite all the adjustments, the transmission parameter in simulations is still higher than the measurements, especially at lower frequencies. This could be explained by the matching being better at these frequencies.

Nevertheless, even with the standard PCB manufacturing tolerances and a cheap FR4 material, measurements confirm that our CLAFSIW design successfully operates in the target frequency band while maintaining a matching below −10 dB. Its transmission characteristics are also similar to the simulated ones, though it shows a 0.45 dB lower value on average between 134 and 148.5 GHz compared to the simulation at a 40-μm gap. At D-band frequencies, the skin depth ($\delta \approx 0.175$ μm at 140 GHz) becomes comparable to the surface roughness of standard PCB copper foils. Therefore, to account for the additional loss, a parametric study of the effective conductivity (σ_{eff}) is performed at a 40-μm gap in Fig. 19. The objective of the approach is to compensate for the effects of surface roughness, which is challenging to characterize directly. The parameter sweep identifies 5.8e^6 S/m of σ_{eff} providing a close alignment between the simulated model and the measurements.

Although calibrating the simulation model to explain prototype behavior is essential to understand the effects of design parameters, ensuring design reproducibility remains equally pivotal. As detailed in Table III, while the prototype dimensions exhibit systematic offsets from the initial simulation model, the statistical variance of the critical parameters across the board remains low. Consequently, precompensating the layout against the manufacturer's systematic offsets, similar to the approach in [29], can effectively ensure predictable operational responses during high-volume manufacturing. Regarding air gap size, replacing mechanical screw assembly with a PCB-compatible adhesive bonding process

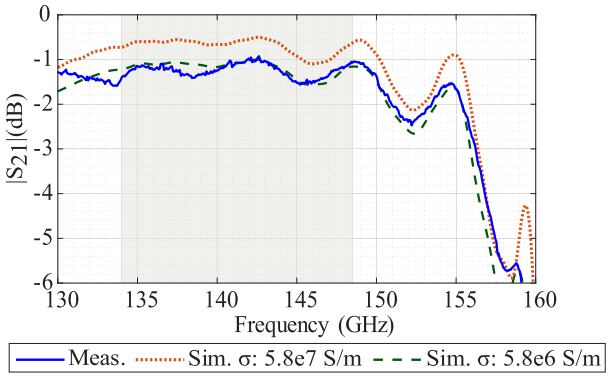


Fig. 19. Comparison of measured (meas.) and simulated (sim.) transmission performance of the design in Fig. 8 with standard (σ: 5.8e^7 S/m) and reduced (σ: 5.8e^6 S/m) copper conductivities and updated dimensions in Table III. The correlation of the effective conductivity model is shown to account for surface roughness effects. Gray rectangle highlights the 134–148.5-GHz band.

(e.g., lamination with a thin prepreg) suitable for mass production can stabilize the gap uniformity and align it closely with predicted values. Crucially, as demonstrated in Fig. 19, the proposed CLAFSIW maintains functional performance across a broader bandwidth than the band of interest. Further matching optimization and the incorporation of process-aware guard bands based on known statistical variations of the design parameters can enable stable performance and high reproducibility during mass production.

To further validate the scalability of our design, we compare the measured performance of two-row straight CLAFSIW lines under different lengths. In Fig. 20(a), the $|S_{21}|$ value decreases as line length increases, which demonstrates that our CLAFSIW design has stable performance regardless of its length. Fig. 20(b) confirms that all designs are well-matched, with an $|S_{11}|$ value below −10 dB across the desired frequency range. The average transmission loss per unit length is estimated by taking the difference between the $|S_{21}|$ of the longest ($L2_2$) and the shortest (T_2) design and averaging across the 134–148.5-GHz range. We then divide the result by the length difference (21.28 mm), giving an estimated loss of 0.037 dB/mm. This differential technique reduces the matching effects and approaches an isolated EBG performance, which is used for comparison with TRL calibration in Section III-C.

Now, we test the wave confinement by comparing the measurements of $L1_2$ and $L1_3$ designs as well as $L2_2$ and $L2_3$ designs. They are well matched with $|S_{11}|$ below −10 dB within the band of interest. Even though two-row designs have slightly fewer reflections, as shown in Fig. 21(a), adding a third row leads to a higher $|S_{21}|$, indicating improved wave confinement and reduced leakage from the waveguide. While this is a beneficial outcome for applications requiring higher confinement, the performance of two-row designs is comparable. Given that our primary goal is a more compact design, we focus on the two-row designs for the remainder of this article.

C. Test Under TRL De-Embedding

In this section, we apply the TRL de-embedding to accurately characterize losses by removing the effects of the

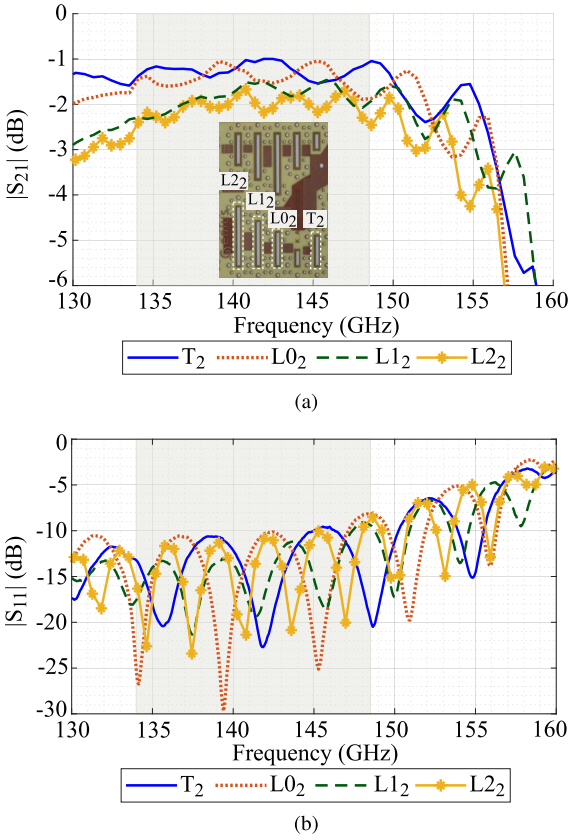


Fig. 20. Measurement comparison of (a) transmission and (b) reflection parameters of two-row straight CLAFSIW designs from the shortest (T_2) to the longest ($L2_2$) length. Each of them is highlighted in the prototype image with white dashed rectangles. The gray rectangle shows the 134–148.5-GHz band.

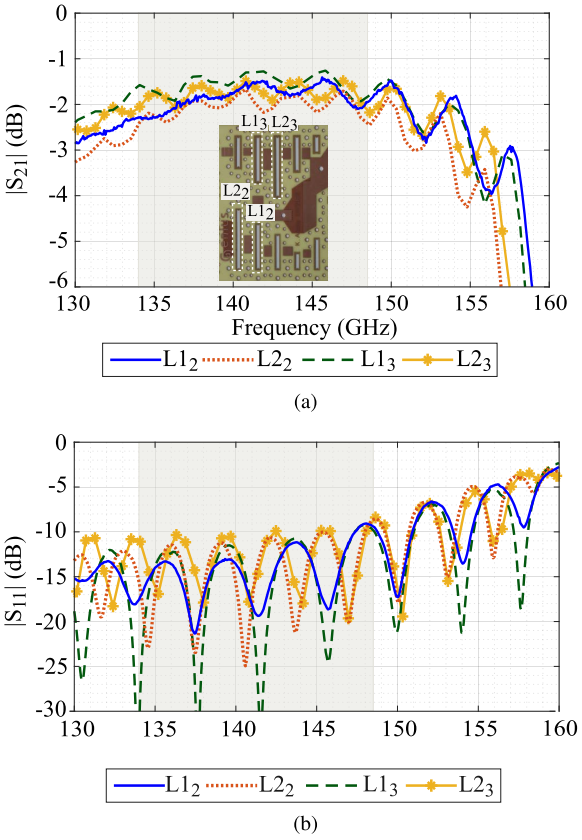


Fig. 21. Measurement comparison of (a) transmission and (b) reflection parameters of two- and three-row approaches for L1 and L2 CLAFSIW designs. Inset prototype image with white dashed rectangles highlighting the analyzed designs. The gray rectangle shows the 134–148.5-GHz band.

TABLE IV
TRANSMISSION LOSS AS A FUNCTION OF FREQUENCY AFTER TRL DE-EMBEDING

f (GHz)	134	137	140	143	146	148.5
$Loss$ (dB/mm)	0.052	0.039	0.037	0.034	0.033	0.030

vertical transition. We use the designs T_2, S_2, and $L0_2$ as thru, reflect, and line standards, respectively. $L0_2$ is made slightly longer than T_2 to achieve a phase value between 20° and 160° in the 134–148.5-GHz band.

Fig. 22 depicts results before and after de-embedding of the design $L2_2$. The raw measurement (meas. $L2_2$) includes the cumulative loss of two vertical transitions and a total length of 42.56 mm ($20\lambda_c$). After de-embedding, the reference planes are shifted inside the waveguide channel, resulting in a length of 21.72 mm ($10.2\lambda_c$), thus exhibiting higher magnitude and significantly reduced oscillations as expected.

The measured transmission losses of CLAFSIW are presented in Table IV. They are performed by dividing the $|S_{21}|$ at each frequency point by the length of 21.72 mm. The design achieves a maximum loss of 0.052 dB/mm at 134 GHz and a minimum loss of 0.03 dB/mm at 148.5 GHz. The average of the measured loss in the operating band is 0.037 dB/mm. It has an excellent alignment with the value estimated in

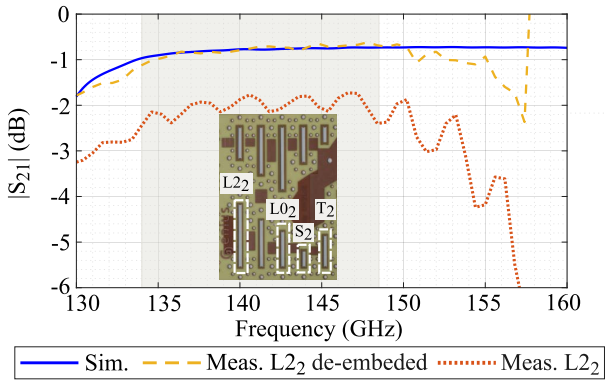


Fig. 22. Comparison between $L2_2$ measurements (meas.) and TRL de-embedded measurements and another simulation (sim.) model fed from sides, excluding vertical transition, at a length of 21.72 mm using updated dimensions in Table III and σ_{eff}: 5.8e^6 S/m.

Section III-B, thereby confirming the performance of our concept using different de-embedding procedures.

In Fig. 22, we compare the measured de-embedded results with another CLAFSIW simulation at the same length using updated dimensions in Table III. The simulation results are obtained by exciting the waveguide from the sides as in Fig. 9 with σ_{eff} = 5.8e^6 S/m. Using the effective conductivity model in Fig. 19 yields great agreement with the de-embedded

TABLE V
AVERAGE LOSS DECOMPOSITION AFTER TRL DE-EMBEDDING

Loss type	*Average* (dB/mm)	% of Total
Ohmic	0.029	78.4%
Dielectric	0.006	16.2%
Leakage	0.002	5.4%
Total	0.037	100%

TABLE VI
COMPARISON BETWEEN CONVENTIONAL TRANSMISSION TECHNOLOGIES

Tech.	Freq. (GHz)	Material	Loss (dB/mm)	Dim. (mm×mm)
Hollow waveguide [8]	110-170	Gold	0.0128 - 0.0081[1]	W: 1.651 H: 0.8255
Microstrip line [14]	135-145	Quartz Gold	0.29	W: 0.03 H: 0.127
SIW [20]	110-170	Ceramic copper	0.155	W: 0.625 H: 0.08
AFSIW [21]	115-155	Air Copper	0.07-0.08	W: 1.6 H: 0.3
MLW [29]	110-170	Air Silver	0.02	W: 1.65 H: 0.64
CLAFSIW (This work)	134-148.5	FR4 copper	0.037	W: 2.24 ∼ H: 0.37

prototype. This provides further validation of our method as a means of accounting for surface roughness.

Therefore, by using the same simulation environment, total loss is decomposed into ohmic, dielectric, and leakage components and summarized in Table V. First, leakage loss is determined by modeling the conductors as perfect electric conductors (PECs) within a lossless dielectric. Dielectric losses are then isolated by applying a lossy dielectric ($tan\delta$ = 0.01) to the PEC model and subtracting the previously calculated leakage. Ohmic losses are derived by implementing the effective conductivity (5.8e^6 S/m) in a lossless dielectric environment excluding leakage. The latter constitutes the vast majority of the total loss (78.4%) while dielectric loss accounts for only 16%, demonstrating the advantage of the air-filled cavity despite the use of FR4. Notably, leakage from the EBG structure represents the minimum loss at merely 5.4%, confirming the effectiveness of mushroom-type UCs for D-band applications.

Here, we remark that a previous work [53] has demonstrated a viable array antenna performance using a PCB-based transmission line with a loss of 0.18 dB/mm at 150-GHz employing laser-drilling and specialized Megtron 7N substrate (ϵ_r: 3.2, tanδ: 0.003). In comparison, the proposed work achieves a loss that is nearly five times lower, significantly enhancing the efficiency of D-band interconnects despite the use of standard manufacturing techniques and materials. In addition, Table VI compares our approach to several published

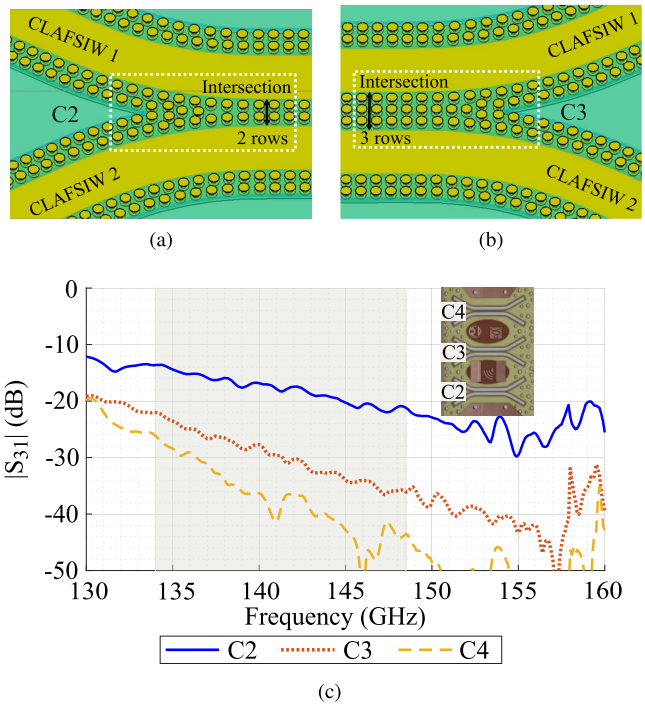


Fig. 23. (a) and (b) Zoomed-in view image of the intersection region (white dashed rectangle) of C2 and C3 designs, respectively. (c) Coupling comparison between de-embedded C2, C3, and C4 designs. The gray rectangle shows the 134–148.5-GHz band.

conventional D-band technologies. It lists the type of technology, the operating band, materials, losses, and the width (W) and height (H) of waveguide channels and microstrip lines. Since these transmission lines utilize diverse materials, making a direct comparison is difficult. Thus, we highlight the performance tradeoffs in different transmission line approaches. By confining the waves within an air-filled cavity, the proposed CLAFSIW achieves lower insertion loss than microstrip lines on quartz or SIW structures on ceramic substrates, despite being fabricated on lossy FR4. Our design is positioned between AFSIW and a silver-plated multilayer waveguide (MLW). Although a fully metallic MLW approach is more advantageous in terms of losses, our approach prioritizes ease of integration to PCB assemblies using high-volume processes and economically scalable materials without significantly compromising D-band performance.

In the context of automotive radar, we benchmark this work against a CNC-milled metallic ridge gap waveguide designed for launcher in package (LiP) applications [45]. The latter achieves an insertion loss of 0.0186 dB/mm at 77 GHz. Considering that conductor losses inherently scale with frequency, the 0.037-dB/mm loss achieved by our proposed design at 140 GHz is highly comparable. Therefore, our FR4-based PCB solution provides an industry-standard efficiency while simultaneously meeting the critical requirements of cost-effectiveness and scalability for D-band automotive radars.

D. Coupling Suppression

We now proceed to investigate the coupling between two intersecting two-row CLAFSIW designs. The analysis

focuses particularly on the intersection region where the number of UC rows varies, as illustrated in the images in Fig. 23(a) and (b). We measure the $|S_{31}|$ parameter highlighting the coupling between Port 1 and Port 3, with matched loads at Ports 2 and 4. Here, we apply the TRL de-embedding to remove the mismatch effects and purely characterize the suppression of the coupling with respect to an increasing number of UC rows at the intersection. The results of this approach are presented in Fig. 23(c). We observe that the coupling linearly decreases in dB scale with each additional row contributing to a more effective isolation. The coupling is substantially reduced, below −13.6, −22, and −26 dB for C2, C3, and C4 configurations, respectively. These results demonstrate the EBG structure robustness in reducing signal interference, even when accounting for manufacturing discrepancies in Table III.

IV. Conclusion and Perspectives

In this article, we demonstrated for the first time a CLAF-SIW concept targeting the 134–148.5-GHz frequency range. The proposed approach proves that a PCB-based solution can effectively operate at D-band while eliminating the need for galvanic contact. The double-layer design is compatible with standard FR4 PCB technology, ensuring simplified fabrication and scalability for mass production. The double-sided mushroom UC, analyzed with MMTMM, maintains a stopband between 127 and 169.7 GHz with a peak attenuation in the target band. The E-bend vertical transition ensures easy integration with microchips based on waveguide launchers and provides an $|S_{11}|$ below −10 dB. Prototype measurements demonstrated valid and satisfactory results that met simulation expectations, confirming a design specifically optimized to maintain performance despite fabrication inaccuracies and sensitivity to the pad size, air-gap, and substrate height. Applying a TRL de-embedding showed 0.037-dB/mm transmission losses on average, providing a competitive performance compared to conventional technologies at D-band. We also showed that the coupling between adjacent structures can be reduced below −26 dB. Overall, our research demonstrated a novel, low-loss and cost-effective transmission line technology capable of confining high-frequency waves, using cheap, lossy materials, and standard manufacturing. This significant practical advantage paves the way for its commercial viability in diverse D-band applications in the automotive industry.

Acknowledgment

The authors would like to thank Dr. Peter Uhlig from IMST GmbH for the dimensional measurements and constructive criticism of this article.

References

[1] I. Bilik, O. Longman, S. Villeval, and J. Tabrikian, "The rise of radar for autonomous vehicles: Signal processing solutions and future research directions," *IEEE Signal Process. Mag.*, vol. 36, no. 5, pp. 20–31, Sep. 2019.

[2] S. S. Ram, "Fusion of inverse synthetic aperture radar and camera images for automotive target tracking," *IEEE J. Sel. Topics Signal Process.*, vol. 17, no. 2, pp. 431–444, Mar. 2023.

[3] IEEE Electronics Packaging Society (EPS). (2021). *Chapter 5: Automotive Heterogeneous Integration Roadmap*. [Online]. Available: https://eps.ieee.org/technology

[4] K. Ramasubramanian and K. Ramaiah, "Moving from legacy 24 GHz to state-of-the-art 77-GHz radar," *ATZelektronik worldwide*, vol. 13, no. 3, pp. 46–49, Jun. 2018, doi: 10.1007/s38314-018-0029-6.

[5] A. Bazzi, F. Miccoli, Z. Wu, F. Cuccoli, and V. Martinez, "A tool for the statistical investigation of the automotive radar interference," in *Proc. 4th URSI Atlantic RadioScience Conf.*, 2024, pp. 1–4.

[6] V. Martinez, A. Filippi, and M. Vlot, "D-band vehicular radars regulatory status," in *Proc. 21st Eur. Radar Conf. (EuRAD)*, Sep. 2024, pp. 276–279.

[7] S. Kueppers, T. Jaeschke, N. Pohl, and J. Barowski, "Versatile 126–182 GHz UWB D-band FMCW radar for industrial and scientific applications," *IEEE Sensors Lett.*, vol. 6, no. 1, pp. 1–4, Jan. 2022.

[8] Virginia Diodes, Inc. (Jun. 2010). *VDI Waveguide Band Designations*. Accessed: May 11, 2026. [Online]. Available: https://vadiodes.com/wp-content/uploads/2009/10/waveguidechart200908.pdf

[9] P.-S. Kildal, E. Alfonso, A. Valero-Nogueira, and E. Rajo-Iglesias, "Local metamaterial-based waveguides in gaps between parallel metal plates," *IEEE Antennas Wireless Propag. Lett.*, vol. 8, pp. 84–87, 2009.

[10] W. Y. Yong, A. Vosoogh, A. Bagheri, C. Van De Ven, A. Hadaddi, and A. A. Glazunov, "An overview of recent development of the gap-waveguide technology for mmWave and sub-THz applications," *IEEE Access*, vol. 11, pp. 69378–69400, 2023.

[11] T. Skaik et al., "Evaluation of 3-D printed monolithic G-band waveguide components," *IEEE Trans. Compon., Packag., Manuf. Technol.*, vol. 13, no. 2, pp. 240–248, Feb. 2023.

[12] M. D'Auria et al., "3-D printed metal-pipe rectangular waveguides," *IEEE Trans. Compon., Packag., Manuf. Technol.*, vol. 5, no. 9, pp. 1339–1349, Sep. 2015.

[13] Y. Zhang, J. Zhang, R. Yue, and Y. Wang, "Loss analysis of thin film microstrip line with low loss at D band," *J. Lightw. Technol.*, vol. 39, no. 8, pp. 2421–2430, Apr. 15, 2021.

[14] G. Guo, T. Zhang, J. Zeng, Z. Yang, L. Yue, and Y. Wei, "Investigation and fabrication of the printed microstrip meander-line slow-wave structures for D-band traveling wave tubes," *IEEE Trans. Electron Devices*, vol. 69, no. 9, pp. 5229–5234, Sep. 2022.

[15] J. Xiao, X. Li, Z. Qi, and H. Zhu, "140-GHz TE_{340} -mode substrate integrated cavities-fed slot antenna array in LTCC," *IEEE Access*, vol. 7, pp. 26307–26313, 2019.

[16] Z.-W. Miao et al., "140 GHz high-gain LTCC-integrated transmit-array antenna using a wideband SIW aperture-coupling phase delay structure," *IEEE Trans. Antennas Propag.*, vol. 66, no. 1, pp. 182–190, Jan. 2018.

[17] J. Xu, Z. N. Chen, X. Qing, and W. Hong, "140-GHz planar broadband LTCC SIW slot antenna array," *IEEE Trans. Antennas Propag.*, vol. 60, no. 6, pp. 3025–3028, Jun. 2012.

[18] A. Altaf and M. Seo, "SIW based D-band single and 2×2 MIMO elliptically tapered slot antenna," *IEEE Access*, vol. 11, pp. 87270–87278, 2023.

[19] Y. Su et al., "140 GHz slow-wave structure loaded SIW miniaturized Butler matrix for multibeam application," in *Proc. IEEE Int. Symp. Radio-Frequency Integr. Technol. (RFIT)*, Aug. 2024, pp. 1–3.

[20] N. Aslani-Amoli et al., "Ultralow-loss substrate-integrated waveguides in alumina ribbon ceramic substrates for 75–170 GHz wireless applications," *IEEE Microw. Wireless Technol. Lett.*, vol. 33, no. 10, pp. 1415–1418, Oct. 2023.

[21] S. Sinha, H. Trischler, I. Ocket, and E. Schaffler, "D-band air-filled substrate integrated waveguide (AFSIW) and broadband stripline to AFSIW launcher embedded in multi-layer PCBs," *IEEE Microw. Wireless Technol. Lett.*, vol. 33, no. 6, pp. 795–798, Jun. 2023.

[22] M. U. Rehman, L. N. V. Kumar, S. Erdogan, and M. Swaminathan, "Air-filled SIWs using laminate dielectrics on glass substrate for D-band applications," *IEEE Trans. Compon., Packag., Manuf. Technol.*, vol. 14, no. 1, pp. 98–105, Jan. 2024.

[23] D. Zarifi, A. Farahbakhsh, and A. U. Zaman, "A gap waveguide-based D-band slot array antenna with interdigital feed network," *IEEE Trans. Antennas Propag.*, vol. 71, no. 9, pp. 7124–7131, Sep. 2023.

[24] J. Liu, A. U. Zaman, and J. Yang, "Two types of high gain slot array antennas based on ridge gap waveguide in the D-band," in *Proc. IEEE-APS Topical Conf. Antennas Propag. Wireless Commun. (APWC)*, Sep. 2019, pp. 75–78.

[25] A. Vosoogh, A. U. Zaman, and V. Vassilev, "Wideband cavity-backed slot subarray with gap waveguide feed-network for D-band applications," in *Proc. 11th Eur. Conf. Antennas Propag. (EUCAP)*, Mar. 2017, pp. 207–209.
[26] A. Farahbakhsh, D. Zarifi, and A. Uz Zaman, "D-band high-gain planer slot array antenna using gap waveguide technology," *IEEE Trans. Antennas Propag.*, vol. 73, no. 1, pp. 594–599, Jan. 2025.
[27] P. Boe et al., "High-precision additive manufacturing of groove gap waveguide filters in D-band," in *Proc. IEEE Asia–Pacific Microw. Conf. (APMC)*, Nov. 2024, pp. 405–407.
[28] J. Zhai, F. Ren, J. Li, and H. Xu, "A D-band contactless wideband transition of ridge gap waveguide and microstrip," in *IEEE MTT-S Int. Microw. Symp. Dig.*, Nov. 2024, pp. 1–3.
[29] A. Vosoogh, H. Zirath, and Z. S. He, "Novel air-filled waveguide transmission line based on multilayer thin metal plates," *IEEE Trans. Terahertz Sci. Technol.*, vol. 9, no. 3, pp. 282–290, May 2019.
[30] Gapwaves AB. *Gapwaves Waveguide Technology*. Accessed: May 11, 2026. [Online]. Available: https://gapwaves.com/waveguide-technology/
[31] K. Aktas, M. Petek, E. Tolin, S. Bruni, and F. Vipiana, "Cost effective PCB gap waveguide based on broken glide symmetry," in *Proc. 19th Eur. Conf. Antennas Propag. (EuCAP)*, Mar. 2025, pp. 1–4.
[32] F. Ghasemifard, F. Mesa, G. Valerio, and O. Quevedo-Teruel, "Propagation characteristics in substrate integrated holey metasurfaces," in *Proc. 14th Eur. Conf. Antennas Propag. (EuCAP)*, Mar. 2020, pp. 1–4.
[33] B. Fischer, J. Sarrazin, and G. Valerio, "Glide-symmetric reconfigurable substrate-integrated holey waveguide," in *Proc. 18th Eur. Conf. Antennas Propag. (EuCAP)*, 2024, pp. 1–4.
[34] D. Sievenpiper, L. Zhang, R. F. J. Broas, N. G. Alexopolous, and E. Yablonovitch, "High-impedance electromagnetic surfaces with a forbidden frequency band," *IEEE Trans. Microw. Theory Techn.*, vol. 47, no. 11, pp. 2059–2074, Nov. 1999.
[35] N. Bayat-Makou and A. A. Kishk, "Contactless air-filled substrate integrated waveguide," *IEEE Trans. Microw. Theory Techn.*, vol. 66, no. 6, pp. 2928–2935, Jun. 2018.
[36] C. Segura-Gómez, Á. Palomares-Caballero, A. Alex-Amor, C. Molero, and P. Padilla, "Air-SIW unit cell with glide-symmetric structures," in *Proc. 17th Eur. Conf. Antennas Propag. (EuCAP)*, Mar. 2023, pp. 1–4.
[37] X. Zhao et al., "High-order resonating cavity-backed slot antenna array based on contactless air-filled substrate-integrated waveguide and transition to inverted grounded coplanar gap waveguide," *IEEE Trans. Antennas Propag.*, vol. 72, no. 12, pp. 8991–9001, Dec. 2024.
[38] A. Amirkabiri, D. Idoko, G. E. Bridges, and B. Kordi, "Contactless air-filled substrate-integrated waveguide (CLAF-SIW) resonator for wireless passive temperature sensing," *IEEE Trans. Microw. Theory Techn.*, vol. 70, no. 7, pp. 3724–3731, Jul. 2022.
[39] M. Sharifi Sorkherizi and A. A. Kishk, "Self-packaged, low-loss, planar bandpass filters for millimeter-wave application based on printed gap waveguide technology," *IEEE Trans. Compon., Packag., Manuf. Technol.*, vol. 7, no. 9, pp. 1419–1431, Sep. 2017.
[40] A. Ugle, M. Casaletti, M. A. Campo, S. Bruni, and G. Valerio, "Stacked multi-via mushroom-type EBG structures with glide symmetry," in *Proc. 19th Eur. Conf. Antennas Propag. (EuCAP)*, Mar. 2025, pp. 1–5.
[41] Z. S. He, A. Hassona, Á. Pérez-Ortega, and H. Zirath, "A compact PCB gasket for waveguide leakage suppression at 110–170 GHz," in *IEEE MTT-S Int. Microw. Symp. Dig.*, Aug. 2020, pp. 888–891.
[42] D. Schwarz, N. Riese, A. Durr, and C. Waldschmidt, "A broadband multilayer vertical transition at 79 GHz employing FR4 as core material," in *Proc. 51st Eur. Microw. Conf. (EuMC)*, Apr. 2022, pp. 700–703.
[43] D. Schwarz, N. Riese, I. Dorsch, and C. Waldschmidt, "System performance of a 79 GHz high-resolution 4D imaging MIMO radar with 1728 virtual channels," *IEEE J. Microw.*, vol. JM-2, no. 4, pp. 637–647, Oct. 2022.
[44] H. U. R. Mohammed, "Advancements in mmWave technology: Launch on package for automotive radars," *Texas* Instruments, Dallas, TX, USA, Tech. Rep. SWRA801, Jan. 2024. [Online]. Available: https://www.ti.com/lit/wp/swra801/swra801.pdf
[45] Q. Ren et al., "Gapwaveguide automotive imaging radar antenna with launcher in package technology," *IEEE Access*, vol. 11, pp. 37483–37493, 2023.
[46] Q. Chen, F. Mesa, X. Yin, and O. Quevedo-Teruel, "Accurate characterization and design guidelines of glide-symmetric holey EBG," *IEEE Trans. Microw. Theory Techn.*, vol. 68, no. 12, pp. 4984–4994, Dec. 2020.
[47] M. Petek et al., "Numerical modeling of higher-symmetric periodic structures with a hexagonal lattice," *IEEE Trans. Antennas Propag.*, vol. 73, no. 3, pp. 1650–1661, Mar. 2025.
[48] F. Giusti, Q. Chen, F. Mesa, M. Albani, and O. Quevedo-Teruel, "Efficient bloch analysis of general periodic structures with a linearized multimodal transfer-matrix approach," *IEEE Trans. Antennas Propag.*, vol. 70, no. 7, pp. 5555–5562, Jul. 2022.
[49] F. Mesa, G. Valerio, R. Rodríguez-Berral, and O. Quevedo-Teruel, "Simulation-assisted efficient computation of the dispersion diagram of periodic structures: A comprehensive overview with applications to filters, leaky-wave antennas and metasurfaces," *IEEE Antennas Propag. Mag.*, vol. 63, no. 5, pp. 33–45, Oct. 2021.
[50] N. P. Gaunkar, G. Dogiamis, T. Kamgaing, A. Elsherbini, and J. Swan, "Multi-layer FCCSP organic packaging for D-band millimeter wave applications," in *Proc. IEEE 72nd Electron. Compon. Technol. Conf. (ECTC)*, May 2022, pp. 365–370.
[51] Panasonic Industry Co. (2022). *Halogen Free R-1566*. Accessed: May 11, 2026. [Online]. Available: https://industrial.panasonic.com/ww/products/pt/halogen-free/hfreer1566
[52] IMST GmbH. (2026). *EMPIRE-Extremely Fast 3D Simulator for Electromagnetic Fields*. Accessed: May 11, 2026. [Online]. Available: https://empire.de/
[53] A. Lamminen, J. Säily, J. Ala-Laurinaho, J. de Cos, and V. Ermolov, "Patch antenna and antenna array on multilayer high-frequency PCB for D-band," *IEEE Open J. Antennas Propag.*, vol. 1, pp. 396–403, 2020.



Kaan Aktaş (Graduate Student Member, IEEE) received the B.Sc. and M.Sc. degrees in electrical engineering from Sorbonne University, Paris, France, in 2021 and 2023, respectively. He is currently pursuing the joint Ph.D. degree with the Politecnico di Torino, Turin, Italy, and IMST GmbH, Kamp-Lintfort, Germany, under the GENIUS Program of the Marie Curie Doctoral Network.

During his academic career, he specialized in electromagnetic theory and microwave engineering. His research interests include metasurfaces, higher symmetric periodic structures, microwave circuits, and radar systems.



Martin Petek (Member, IEEE) received the B.Sc. degree in electrical engineering from the University of Ljubljana, Ljubljana, Slovenia, in 2017, the M.Sc. degree in electrophysics from the KTH Royal Institute of Technology, Stockholm, Sweden, in 2020, and the Ph.D. degree (cum laude) from the Politecnico di Torino, Turin, Italy, in 2025.

He is currently at the Department of Electronics and Telecommunications, Politecnico di Torino, as a Post-Doctoral Researcher. His current research interests include numerical techniques, periodic structures, and higher symmetries.



Enrico Tolin received the M.Sc. degree in electronic engineering from the Università degli Studi di Padova, Padua, Italy, in 2008, and the Ph.D. degree in electrical, electronics and communications engineering from the Politecnico di Torino, Turin, Italy, in 2020.

From 2010 to 2014, he was a Research and Development Engineer with Calearo Antenne S.p.A, Vicenza, Italy. Since 2014, he has been a part of the Antennas and EM Modeling Group, IMST GmbH, Kamp-Lintfort, Germany. His current research interests include the design of reconfigurable antennas and systems, integrated antennas, antenna arrays, active and passive circuits, and low-noise amplifiers.



Simona Bruni (Member, IEEE) was born in Civitavecchia, Italy. She received the M.S. degree in telecommunication engineering and the Ph.D. degree in electromagnetics from the University of Siena, Siena, Italy, in 2002 and 2006, respectively.

From 2005 to 2007, she was a Researcher Financed and hosted by the Defense, Security and Safety Institute, Netherlands Organization for Applied Scientific Research (TNO), The Hague, The Netherlands. From 2007 to 2013, she was a Research and Development Antenna Engineer with the Calearo Advanced Technology (CAT) Department, Calearo Antenne S.p.A (later acquired by MTA), Vicenza, Italy. Since 2013, she has been a Research and Development Antenna Engineer at the Antenna Front-Ends Team, Antennas and EM Modeling Department, IMST GmbH, Kamp-Lintfort, Germany. She co-authored this article that received the Best Applied Technology Antenna Paper Award from European Conference on Antennas and Propagation (EuCAP) in 2023. Since 2026, she has been a member of the Advisory Board for the Department of Electronics and Telecommunications (DET), Politecnico di Torino, Turin, Italy. Since 2026, she has been the Technical Co-Director of Sub-THz Antenna Systems with IMST GmbH. Her research is dedicated to advanced integrated antennas, high-frequency antenna arrays, and front-end designs, with a strong focus on communication, sensing, and automotive systems.



Jorge Alberto Tobón Vásquez received the bachelor's degree in electronics engineering from the Universidad de Antioquia, Medellín, Colombia, in 2010, and the master's and Ph.D. degrees in electronics and telecommunication from the Politecnico di Torino, Turin, Italy, in 2010 and 2014, respectively.

Since 2024, he has been at Wavision S.r.l., Turin, Italy, (Politecnico di Torino spin-off). His main research activities correspond to modeling, designing, and analyzing systems for microwave imaging applications, and the numerical modeling of complex and nonhomogeneous media propagation.

Dr. Vásquez received the "Premio Latmiral," an award granted by Italian Society of Electromagnetism (SIEM) in 2018. In 2020, he received the URSI General Assembly Scientific Symposium (GASS) Young Scientist Award (YSA) and the Sorrentino URSI Italy National Meeting Young Scientist Paper Award.



Francesca Vipiana (Senior Member, IEEE) received the Laurea and Ph.D. degrees in electronic engineering from the Politecnico di Torino, Turin, Italy, in 2000 and 2004, respectively, with doctoral research carried out partly at European Space Research Technology Center, Noordwijk, The Netherlands.

From 2005 to 2008, she was a Research Fellow with the Department of Electronics, Politecnico di Torino. From 2009 to 2012, she was the Head of the Antenna and EMC Laboratory, Istituto Superiore Mario Boella, Turin. Since 2012, she has been an Assistant Professor with the Department of Electronics and Telecommunications, Politecnico di Torino, where she has been an Associate Professor since 2014 and a Full Professor since 2021. Her main research activities concern numerical techniques based on integral equations and the method of moments, with a focus on multiresolution and hierarchical schemes, domain decomposition, preconditioning and fast solution methods, advanced quadrature integration schemes, and analysis of glide-periodic structures. Moreover, her research interests include the modeling, design, realization, and testing of microwave imaging and sensing systems for medical and industrial applications.

Dr. Vipiana is a member of the EurAAP Board of Directors and the Vice-Chair of the IEEE AP-S Expanding Collaboration and Engagement (ECE) Committee. She received the Lot Shafai Mid-Career Distinguished Award from the IEEE Antennas and Propagation Society (AP-S) in 2017, the Best Paper Award at Spanish URSI Symposium in 2023, and the Best Electromagnetics Paper Award at the 20th European Conference on Antennas and Propagation (EuCAP) in 2026. She was an Associate Editor of IEEE TRANSACTIONS ON ANTENNAS AND PROPAGATION (2018–2024) and the Founder and responsible for the Women in Engineering Column in *IEEE Antennas and Propagation Magazine* (2019–2024).

Open Access funding provided by 'Politecnico di Torino' within the CRUI CARE Agreement